Solid State Communications 254 (2017) 31–36

Contents lists available at ScienceDirect

Solid State Communications

journal homepage: www.elsevier.com/locate/ssc

Communication

# Lattice dynamics and thermal conductivity of cesium chloride via first-principles investigation

Cui He[a], Cui-E Hu[b], Tian Zhang[a], Yuan-Yuan Qi[c], Xiang-Rong Chen[a,*]

[a] Institute of Atomic and Molecular Physics, College of Physical Science and Technology, Sichuan University, Chengdu 610065, China
[b] College of Physics and Electronic Engineering, Chongqing Normal University, Chongqing 400047, China
[c] College of Science, Henan University of Technology, Zhengzhou 450001, China

ARTICLE INFO

Communicated by F. Peeters

*Keywords:*
Lattice thermal conductivity
Phonon spectrum
Density functional theory

ABSTRACT

The lattice thermal conductivity of CsCl crystal is theoretically investigated from a first-principles theoretical approach based on an iterative solution of the Boltzmann transport equation. Real-space finite-difference supercell approach is employed to generate the harmonic and anharmonic interatomic force constants. Phonon frequencies, velocities, and specific heat capacity as well as anharmonic properties are then obtained and applied to calculate the bulk thermal conductivity of CsCl crystal at the temperatures ranging from 20 K to 700 K. The calculated lattice thermal conductivity 1.14 W/mK of CsCl at room temperature agrees well with the experimental value, demonstrating that this parameter-free approach can provide a good description for the thermal transport of this material. The RTA and iterative solution of BTE are both presented. Our results show that both methods can obtain the thermal conductivity successfully.

## 1. Introduction

Cesium chloride (CsCl), a family member of alkali halides (AH), is one of the most popular and important materials. Its special structure usually induces some interesting electro-optic properties, electro-mechanic properties, and large dielectric constants, etc. [1]. The finding of colour centres in CsCl [2] is promising for applications in new optical devices, such as waveguides and nanolaser. These potential applications are closely relative with an good understanding of thermal transport property, and a low lattice thermal conductivity of CsCl can greatly promote their performances. It is noted that some AH, such as LiF and NaF with rather low thermal conductivity [3,4], can be good candidates for coolants and solvents in the next generation of nuclear fission reactors [5]. Thus it is important to get reliable data on the thermal properties of AH for evaluating their capabilities as coolants. However, the researches on the thermal transport of CsCl are scarce due to the difficulties in the experimental determinations and the imperfect theoretical approaches. Based on the transient hot wire method, the thermal conductivity (about 1.01 W/mK) of CsCl were measured by Gerlich and Andersson in 1982 [6], however, up to now there are not other relative experiments or theoretical studies on the thermal transport of CsCl, as greatly limits its applications.

Nonmagnetic crystals' heat carriers are electrons and phonons, with phonons dominating heat transport in semiconductors and insulators. For the phonon thermal conductivity, a popular accepted approach is to solve the Boltzmann transport equation (BTE), which was originally formulated by Peierls in 1929 [7]. Then, more and more methods were carried out, such as relaxation time approximation (RTA) [8,9] and Callway's model [10,11]. The RTA is derived assuming elastic scattering, which indicates that umklapp (U) and normal (N) scattering processes are independent, and both of them provide resistive manner. This is contradicting because in practice, U scattering process can provide the thermal resistive manner but N scattering process can not [12]. In addition, the involved parameters in the Callway's model can only be obtained by fitting the experimental data. Thus the above methods have limited power.

In recent years, ShengBTE [13] code based on a full iterative solution to the linearized phonon BTE has been achieved free of adjustable parameters, which uses only basic structure information and the only inputs are the harmonic and anharmonic interatomic force constants (IFCs). To date, ShengBTE calculations of thermal conductivity have been applied to many systems successfully [14–17]. Thus in this work, we will use the ShengBTE code to study the lattice thermal conductivity and related physical quantities of CsCl crystal. In Section 2, the theoretical methods and calculation details are presented. Some results and discussion are presented in Section 3. Finally, we summarize the calculated results in Section 4.

* Corresponding author.
*E-mail address:* xrchen@scu.edu.cn (X.-R. Chen).

http://dx.doi.org/10.1016/j.ssc.2016.12.004
Received 5 September 2016; Received in revised form 5 November 2016; Accepted 8 December 2016
Available online 09 December 2016

## 2. Theoretical methods and calculation details

A non-zero heat current $J$ can arise from a temperature gradient $\nabla T$. In the linear regime, the components of $\kappa$ are defined by the equation, $J^{\alpha} = -\sum_{\beta} \kappa^{\alpha\beta}(\nabla T)^{\beta}$, where $J$ can be expressed as [13]

$$J = \sum_{p} \int f_{\lambda}\, \hbar\omega_{\lambda} v_{\lambda} \frac{d\mathbf{q}}{(2\pi)^3}, \tag{1}$$

where $\lambda$ composes both a phonon branch index $p$ and a wave vector $\mathbf{q}$, $\omega_{\lambda}$ and $v_{\lambda}$ are the angular frequency and the group velocity of phonon mode $\lambda$, respectively. $f_{\lambda}$is the phonon distribution function. Phonons are distributed according to Bose–Einstein statistics $f_0(\omega_{\lambda})$ at thermal equilibrium. In the presence of a temperature gradient $\nabla T$, the phonon distribution $f_{\lambda}$ deviates from $f_0$ and the deviation can be obtained from the phonon BTE,

$$-\nabla T \cdot v_{\lambda} \frac{\partial f_{\lambda}}{\partial t} + \left.\frac{\partial f_{\lambda}}{\partial t}\right|_{scattering} = 0, \tag{2}$$

where the first term is the diffusion term due to the temperature gradient, and the second term is the scattering term determined by the phonon-phonon interactions and the impurities (such as isotopes).

When the scattering sources are only the two- and three-phonon processes, the resulting linearized BTE can then be written as [18,19]

$$F_{\lambda} = \tau_{\lambda}^{0}(v_{\lambda} + \Delta_{\lambda}), \tag{3}$$

where $\tau_{\lambda}^{0}$ is the relaxation time of mode $\lambda$, as obtained from perturbation theory. In fact, setting all $\Delta_{\lambda}$ to zero is equivalent to working within the RTA. $\Delta_{\lambda}$ and $\tau_{\lambda}^{0}$ are computed as [13]

$$\mathbf{\Delta}_{\lambda} = \frac{1}{N}\sum_{\lambda'\lambda''}^{+} \Gamma^{+}_{\lambda\lambda'\lambda''}(\xi_{\lambda'\lambda''}\mathbf{F}_{\lambda''} - \xi_{\lambda\lambda'}\mathbf{F}_{\lambda'}) + \frac{1}{N}\sum_{\lambda'\lambda''}^{-} \frac{1}{2}\Gamma^{-}_{\lambda\lambda'\lambda''}(\xi_{\lambda'\lambda''}\mathbf{F}_{\lambda''} + \xi_{\lambda\lambda'}\mathbf{F}_{\lambda'}) + \frac{1}{N}\sum_{\lambda'} \Gamma_{\lambda\lambda'}\xi_{\lambda\lambda'}\mathbf{F}_{\lambda'} \tag{4}$$

$$\frac{1}{\tau_0} = \frac{1}{N}\left(\sum_{\lambda'\lambda''}^{+} \Gamma^{+}_{\lambda\lambda'\lambda''} + \sum_{\lambda'\lambda''}^{-} \frac{1}{2}\Gamma^{-}_{\lambda\lambda'\lambda''} + \sum_{\lambda'} \Gamma_{\lambda\lambda'}\right), \tag{5}$$

where the discretization of the Brillouin zone (BZ) is introduced into a Γ-centered regular grid of $N{=}N_1{\times}N_2{\times}N_3$ q points, and the shorthand $\xi_{\lambda\lambda'} = \omega^{\lambda'}/\omega^{\lambda}$ is used.

The three-phonon scattering rates $\Gamma^{\pm}_{\lambda\lambda'\lambda''}$ in Eq. (5) can be expressed as [13]

$$\Gamma^{+}_{\lambda\lambda'\lambda''} = \frac{\hbar\pi}{4}\frac{f_0' - f_0''}{\omega_{\lambda}\omega_{\lambda'}\omega_{\lambda''}}\left|V^{+}_{\lambda\lambda'\lambda''}\right|^2 \delta(\omega_{\lambda} + \omega_{\lambda'} - \omega_{\lambda''}), \tag{6}$$

$$\Gamma^{-}_{\lambda\lambda'\lambda''} = \frac{\hbar\pi}{4}\frac{f_0' + f_0'' + 1}{\omega_{\lambda}\omega_{\lambda'}\omega_{\lambda''}}\left|V^{-}_{\lambda\lambda'\lambda''}\right|^2 \delta(\omega_{\lambda} - \omega_{\lambda'} - \omega_{\lambda''}), \tag{7}$$

where $\Gamma^{+}_{\lambda\lambda'\lambda''}$ corresponds to the absorption processes, and two incident phonons result in only one phonon ($\omega_{\lambda} + \omega_{\lambda'} = \omega_{\lambda''}$), whereas $\Gamma^{-}_{\lambda\lambda'\lambda''}$ describes the emission processes, in which the energy of one phonon split among two phonons ($\omega_{\lambda} - \omega_{\lambda'} = \omega_{\lambda''}$). For simplicity, $f_0'$ stands for $f_0(\omega_{\lambda'})$ and so forth. Conservation of energy in the absorption and emission processes is enforced by the Dirac delta distributions in Eqs. (6) and (7). To successfully compute the values of $\Gamma^{\pm}_{\lambda\lambda'\lambda''}$, we need the scattering matrix elements $V^{\pm}_{\lambda\lambda'\lambda''}$ given by

$$V^{\pm}_{\lambda\lambda'\lambda''} = \sum_{i\in u.c.}\sum_{j.k}\sum_{\alpha\beta\gamma} \Phi^{\alpha\beta\gamma}_{ijk} \frac{e^{\alpha}_{\lambda}(i)\, e^{\beta}_{p',\pm\mathbf{q}'}(j)\, e^{\gamma}_{p'',-\mathbf{q}''}(k)}{\sqrt{M_i M_j M_k}}, \tag{8}$$

which in turn depends on the normalized eigenfunctions $e_{p,q}$ of the involved three phonons and the anharmonic IFCs $\Phi^{\alpha\beta\gamma}_{ijk}$, that can be calculated by a supercell-based finite-difference method

$$\Phi^{\alpha\beta\gamma}_{ijk} = \frac{\partial^3 E}{\partial r_i^{\alpha}\partial r_j^{\beta}\partial r_k^{\gamma}} \approx \frac{1}{2h}\left[\frac{\partial^2 E}{\partial r_j^{\beta} r_k^{\gamma}}(r_i^{\alpha} = h) - \frac{\partial^2 E}{\partial r_j^{\beta} r_k^{\gamma}}(r_i^{\alpha} = -h)\right]$$
$$\approx \frac{1}{4h^2}[-F_k^{\gamma}(r_i^{\alpha} = h,\, r_j^{\beta} = h) + F_k^{\gamma}(r_i^{\alpha} = h,\, r_j^{\beta} = -h)]$$
$$+ F_k^{\gamma}(r_i^{\alpha} = -h,\, r_j^{\beta} = h) - F_k^{\gamma}(r_i^{\alpha} = -h,\, r_j^{\beta} = -h), \tag{9}$$

where $h$ is a small displacement from the equilibrium position, $F_k^{\gamma}$ is the γ component of the force suffered by the $k$-th atom. $k_l$ can be obtained in terms of $F$ as

$$\kappa_l^{\alpha\beta} = \frac{1}{k_B T^2 \Omega N}\sum_{\lambda} f_0(f_0 + 1)(\hbar\omega_{\lambda})^2 v_{\lambda}^{\alpha}\mathbf{F}_{\lambda}^{\beta}, \tag{10}$$

where $\Omega$ is the volume of the unit cell. In ShengBTE implement, Eq. (3) is starting with a zeroth-order approximation $\mathbf{F}_{\lambda}^{0} = \tau_{\lambda}^{0}\mathbf{v}_{\lambda}$, and stopping criterion is that the relative change in the calculated conductivity tensor is less than a configurable parameter. Stopping at the zeroth iteration is equivalent to operating under RTA. In addition, a number of related physical quantities can also be computed to provide additional insight. The most representative is the specific heat per unit volume $C_{\upsilon}$, the scalar mean free path $\Lambda_{\lambda}$ for mode $\lambda$, and the mode-averaged Gruneisen parameter, which are given by

$$C_{\upsilon} = \frac{k_B}{\Omega N}\sum_{\lambda}\left(\frac{\hbar\omega}{k_B T}\right)^2 f_0(f_0 + 1) = \frac{k_B}{(2\pi)^3}\int_{BZ}\left(\frac{\hbar\omega}{k_B T}\right)^2 f_0(f_0 + 1)\, d^3\mathbf{q}. \tag{11}$$

$$\Lambda_{\lambda} = \frac{\mathbf{F}_{\lambda}\cdot\mathbf{v}_{\lambda}}{|\mathbf{v}_{\lambda}|}. \tag{12}$$

$$\bar{\gamma} = \sum_{\lambda} C_{\lambda}\gamma_{\lambda} / \sum_{\lambda} C_{\lambda}. \tag{13}$$

We performed the structural optimization using the Vienna Ab-initio Simulation Package (VASP) [20]. Local-density approximation (LDA) proposed by Vosko et al.[21] and generalized gradient approximation (GGA) proposed by Perdew et al. [22] with the projector augmented wave (PAW) pseudopotentials [23] have been used to calculate the equilibrium lattice constant. A plane-wave cut-off of 450 eV with a 9×9×9 Monkhorst-Pack grid [24] of k-point sampling was used to relax the structure, and the energy convergence threshold was set as $10^{-8}$ eV. It is found that GGA overestimate the equilibrium lattice constant and LDA underestimate it. Our LDA result (4.039 Å) is closer to the experimental value (4.10 Å [25]) than our GGA result (4.225 Å), and also agree with other theoretical data, 3.99 Å [26] and 4.085 Å [27]. In the following, we use LDA method to investigate the phonon and thermal properties of CsCl crystal.

These parameters above were used for our calculations of the second-order and the third-order IFCs. The second-order and third-order IFCs were calculated using the real space supercell approach based on the equalized unit cell, where the IFCs are approximated by the finite differences of forces [28]. For the third-order IFCs, a cut-off of the interaction range is such that atoms up to the 3rd nearest neighbors are included. Then the phonon dispersion and dielectric parameters (dielectric tensor and Born effective charges) were calculated using the density functional perturbative theory (DFPT) in VASP and Phonopy [29] based on a 3×3×3 supercell. Finally, the linearized BTE was iteratively solved through ShengBTE code.

## 3. Results and discussion

### 3.1. Lattice dynamics and phonon spectra

The obtained phonon dispersion relation along several high-symmetry lines for CsCl crystal is shown in Fig. 1. Since the primitive unit cell of CsCl contains two nonequivalent atoms, six independent vibration modes can be found, three of which are acoustic modes (two transverse and one longitudinal) and the remaining three are optical modes. In Fig. 1, the blue lines and the red stars represent the

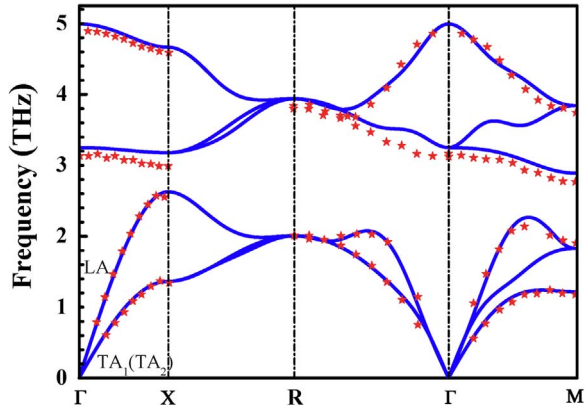


**Fig. 1.** Phonon dispersion relation of CsCl. Blue lines: the present calculation; Red stars: the neutron scattering data by Ahmad et al. [30]. (For interpretation of the references to color in this figure legend,the reader is referred to the web version of this article)

present results and the neutron scattering experimental data by Ahmad et al.[30], respectively. It can be seen that two transverse acoustical branches (TA1, TA2) and two transverse optical branches are degenerate along the symmetrical directions (from Γ to X and from Γ to R) inside the Brillouin zone. The directions from Γ to X and from Γ to R are more symmetrical than other directions. When the symmetry is broken, the degeneracy in the modes disappears. It is well-known that the famous tendency of LDA method is to underestimate the bond lengths and overestimate the bond energies. Since the harmonic and anharmonic IFCs are derivatives of the energy, the LDA calculations will generally overestimate the optic phonon frequency and the scattering rate while the GGA calculations will generally underestimate the optic phonon frequency and the scattering rate [31]. In fact, this over- or under-estimated tendency for phonon frequencies can also be found in other theoretical results. The phonon spectra of GaN and diamond calculated by Ward et al.[12] and Lindsay et al.[32] based on LDA method showed that their frequencies are overestimated when compared with their corresponding experimental data. Furthermore, Favot et al.[33] made a detailed calculation for the phonon spectra of the covalently bonded solid diamond and the metal Cu based on LDA and GGA methods. They also found that LDA method overestimates the phonon frequency and GGA method underestimates the phonon frequency. Based on these theoretical results, we think that our overestimated phonon frequencies with LDA method are reasonable. Overall, our LDA calculations have a high degree of agreement with the experimental data. The accurate phonon dispersion in this work confirms the reliability of the harmonic IFCs calculations.

The Born effective charges and dielectric constant, which are required to resolve the longitudinal and transverse optical phonon (LO-TO) splitting at the Γ point, were also evaluated using the density functional perturbation theory. The results obtained are all listed in Table 1, together with other theoretical data [34] and the experimental data [35,36]. It can be seen that our dielectric constant and Born effective charges agree better with the corresponding experimental data than the theoretical results by LDA method plus norm-conserving pseudopotentials of Hong and Vanderbilt [34]. This agreement suggests that the projector augmented wave (PAW) pseudopotentials seem to be better than the norm-conserving pseudopotentials for this material. Furthermore, both the dielectric constant and Born effective charges obtained by us and by Hong and Vanderbilt [34] are higher than the experimental data. In fact the corresponding work about the overestimated dielectric constant by LDA method has also been reported by Baroni and Resta [37]. The center of Brillouin zone phonon frequencies are also listed in Table 1, together with other theoretical data [1] and the experimental data [30,35]. It is found that the results by Bingol et al.[1] based on GGA method plus linearized PAW pseudopotentials are larger than the experimental data, and their

**Table 1**
The dielectric constant $\varepsilon$, Born effective charges, and the center of Brillouin zone phonon frequencies $\omega$ ($cm^{-1}$) of CsCl crystal, together with other theoretical data and the experiment data.

| CsCl | Present work | Other theoretical data | Experiment data |
|---|---|---|---|
| $\varepsilon$ | 3.125 | 3.2[a], | 2.6927[b] |
| $Z^*$ (Cs) | 1.3441 | 1.36[a], | 1.26[c] |
| $Z^*$ (Cl) | −1.3445 | −1.36[a] | −1.26[c] |
| $\omega_{LO}$ | 166 | 182[d] | 165[b],163[e] |
| $\omega_{TO}$ | 108 | 132[d] | 99[b],104[e] |

[a] The local-density approximation plus Norm-conserving pseudopotentials by Hong et al.[34];
[b] The transmission and reflexion experiment data by Jones et al. [35];
[c] The experimental data obtained by Born et al.[36];
[d] The GGA approximation plus linearized PAW pseudopotentials by Bingol et al.[1];
[e] Inelastic neutron-scattering data by Ahmad et al.[30];

deviations are even over our theoretical results, indicating that this reliability of the theoretical results by Bingol et al.[1] has some doubt.

### 3.2. Phonon mean free path and scattering rates

The cumulative lattice thermal conductivity with the allowed maximum mean free path (MFP) $\Lambda_{max}$ at room temperature is shown in Fig. 2, where the solid black line represents our results. The similarity of the curve to a logistic function, when plotted with the horizontal axis in the logarithmic scale, suggests a fit to a nonparametric function in the form

$$\kappa_l(\Lambda \le \Lambda_{max}) = \kappa_l \Big/ \left(1 + \frac{\Lambda_\lambda}{\Lambda_{max}}\right). \tag{14}$$

where $\Lambda_\lambda$ is the mean free path. This fit is shown as a dashed red line in Fig. 2. It yielded mean free path $\Lambda_\lambda = 9.4$ nm that can be interpreted as representative of the mean free path of relevant heat-carrying phonons in bulk CsCl crystal. This is important when designing nanostructure approaches to reducing $k_l$, for instance with thermoelectric applications in mind. However, it is regrettable that we do not find other theoretical data for our comparison.

In Fig. 3, we plot the phonon mean free path $\Lambda_\lambda$ at different temperatures ranging from 20 K to 700 K. It can be seen that the phonon mean free path $\Lambda_\lambda$ sensitively depends on temperatures. At extremely low temperatures, the phonon-phonon scattering's umklapp processes are weak, and the phonon mean free path $\Lambda_\lambda$ is determined by crystal size. Thus, $\Lambda_\lambda$ is large at lower temperatures. As the temperature rises, the umklapp processes increase, and the phonon mean free path is reduced. At higher temperatures, $\Lambda_\lambda$ tends to be inversely propor-

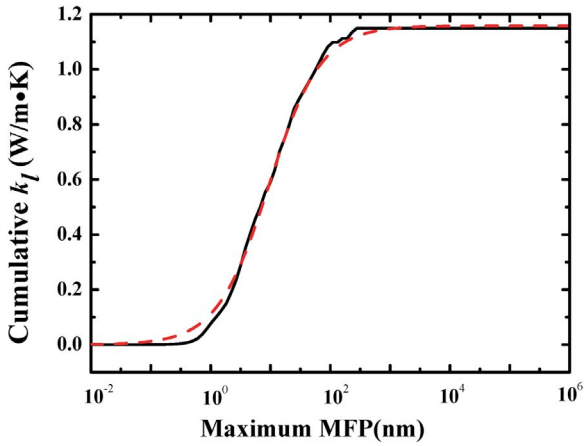


**Fig. 2.** Cumulative lattice thermal conductivity $\kappa_l$ of CsCl as a function of the maximum mean free path at 300 K. Solid black line: our results; Dashed red line: fit to a function of the form described by Eq. (14).

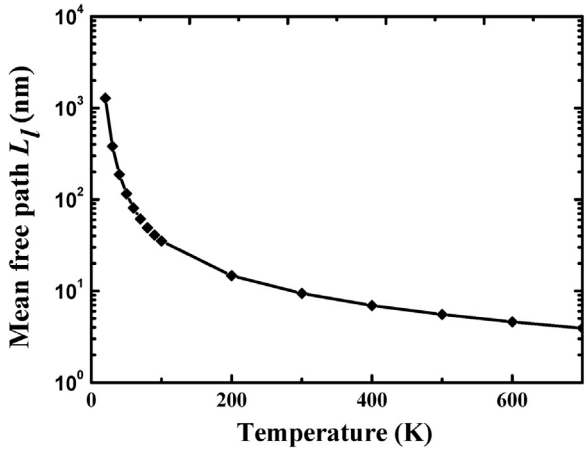


**Fig. 3.** Phonon mean free path of CsCl at the temperatures ranging from 20 K to 700 K.

tional to temperature.

The total converged phonon scattering rates of CsCl crystal at room temperature are shown in Fig. 4. The black rectangles, blue cycles and red triangles represent the acoustic phonons modes, the others represent the optical modes. We note that there is a gap between acoustic and optical branches, which is in accord well with the above phonon spectra. Although the scattering rate of three acoustic branches rises with the increasing frequency, it is still lower than the optical phonons' scattering rate in general.

Fig. 5 illustrates each mode and the irreducible q-point's dimensionless scattering phase space volume ($P_3^j(q)$). $P_3^j(q)$, introduced by Weber [38], employs an adiabatic bond charge model (ABCM) and satisfies energy and momentum conservation in the three phonon scattering processes. We can see from Fig. 5 that the phase space volumes of the acoustic modes are larger than those of the optical modes. The decrease of the phase space volumes from acoustic modes to optical modes is due to the gap, because the gap can suppress the interaction of acoustic phonons with optical phonons over the gap. In addition, we also obtain the contributions to thermal conductivities from different phonon branches. Our results indicate that the contribution of acoustic modes is about 90%, which is far more than those from optical modes, and the contribution of longitudinal acoustic phonon modes is the largest when compared with other modes. This

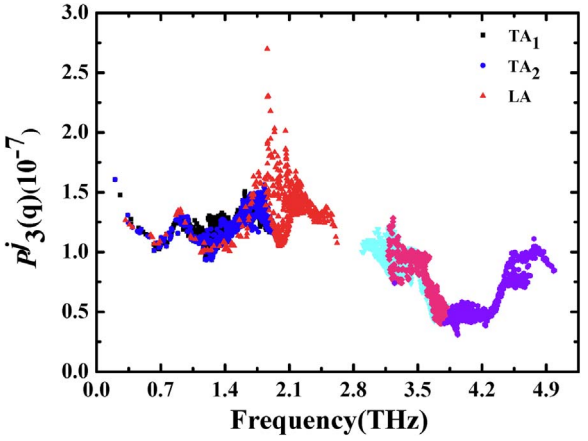


**Fig. 5.** Dimensionless phase space volume available for each mode (j) and irreducible q-point (q) to participate in three-phonon scattering processes at 300 K, computed on a 27×27×27 **q**-point grid and scalebroad=1.0. Phonon branches are denoted by colors. The black rectangles, blue cycles and red triangles are acoustic phonons modes, and others are optic modes. (For interpretation of the references to color in this figure legend,the reader is referred to the web version of this article)

result accords with the conclusion that the acoustic modes dominate the thermal transport [39].

It is known that the total phase space $P_3$ have a strong negative correlation with thermal conductivity $k$[40]. The obtained total phase space $P_3$ of CsCl about $1.2\times10^{-2}$ $eV^{-1}$ at room temperature is higher than the $P_3$value of $0.94\times10^{-2}$ $eV^{-1}$ for CdTe [41], but is lower than the $P_3$value of $1.9\times10^{-2}$ $eV^{-1}$ for SnSe [40]. Thus we can think that the $k$ value of CsCl must be between the $k$ value of 0.54 W/(m K) [41] for SnSe and the $k$ value of 7.5 W/(m K) [40] for CdTe.

### 3.3. Heat capacity and thermal conductivity

The heat capacity per unit volume ($C_v$) of CsCl crystal at 300 K are shown in Table 2 together with the experimental data [6] and the heat capacity obtained from the thermal expansion data [42]. It can be seen that our heat capacity $C_v$ show good agreement with the experimental data and the theoretical data. The temperature dependence of $C_v$ are plotted in Fig. 6, where the black squares, red stars and blue triangles represent the present results, the experimental data, and the heat

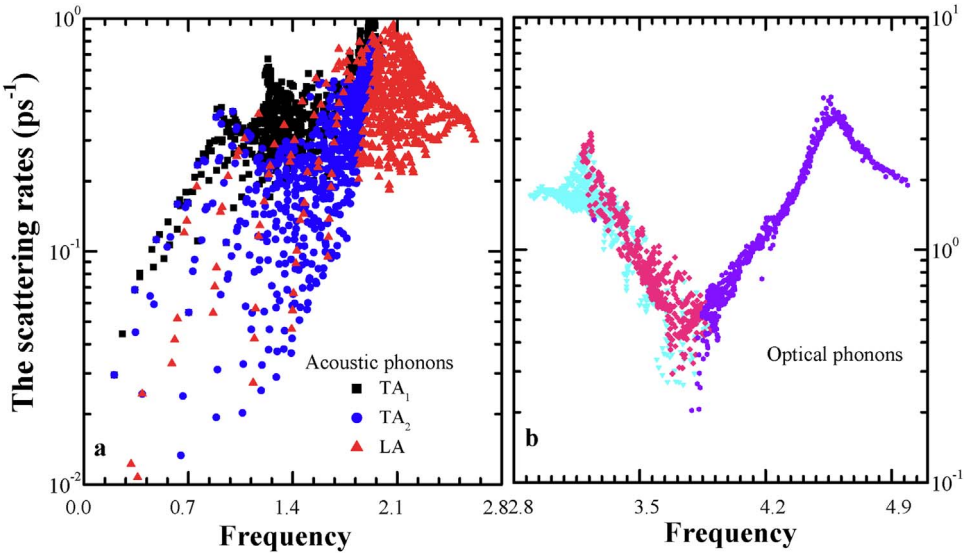


**Fig. 4.** Phonon scattering rates of CsCl at room temperature, computed on a 27×27×27 **q**-point grid and scalebroad=1.0. Phonon branches are denoted by colors. (a) Phonon scattering rate of acoustic phonons. The black rectangles, blue cycles and red triangles are $TA_1$, $TA_2$, LA, respectively. (b) Phonon scattering rate of optical phonons. (For interpretation of the references to color in this figure legend,the reader is referred to the web version of this article)

**Table 2**
The calculated heat capacity per unit volume $C_v$, phonon mean free path $\Lambda_\lambda$ and thermal conductivity $\kappa_l$ of CsCl at 300 K, together with the experimental and other theoretical data.

| CsCl | Present work | Exp. | Other theoretical data |
|---|---|---|---|
| $C_v$/MJ/(m$^3$ K) | 1.28 | 1.23[a] | 1.25[b] |
| $\bar{\gamma}$ | 1.92 | | 2.05[a] |
| $\kappa_l$/W/(m K) | 1.08[c], 1.14[d] | 1.01[a] | |

[a] The measured data from Gerlich and Andersson at 300 K [6];
[b] The obtained data from the expansion data by Touloukian et al.[42];
[c] Present result from the RTA;
[d] Present result from the iterative solutions of BTE.

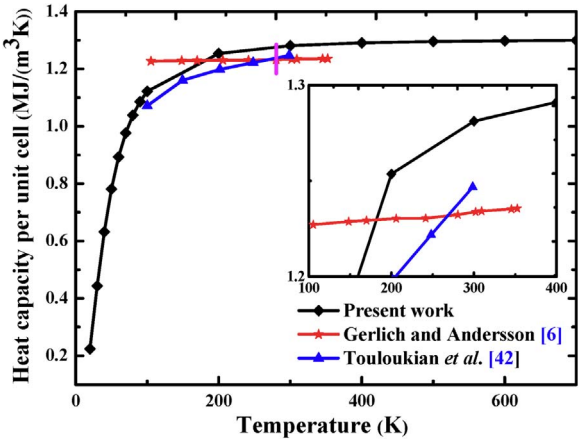


**Fig. 6.** Heat capacity per unit volume $C_v$ of CsCl at different temperatures ranging from 20 K to 700 K. The inset figure is heat capacity per unit volume $C_v$ of CsCl at different temperatures ranging from 100 K to 400 K. The black square, red stars and blue triangles are our present result, the neutron scatter data [6] and the data obtained from the thermal expansion data [42]respectively. The magenta line is the experimental error bars, indicating the maximum scatter of the experimental data points. (For interpretation of the references to color in this figure legend,the reader is referred to the web version of this article)

capacity obtained from the thermal expansion data, respectively. The magenta line is the experimental error bars, indicating the maximum scatter of the experimental data points. It can be seen that the heat capacity $C_v$ rapidly increases with the rise of temperature $T$ at low temperature and is proportional to $T^3$, whereas it tends to be a constant value at high temperatures, following the Dulong-Petit law. The inset figure in Fig. 6 is the heat capacity $C_v$ of CsCl crystal at temperatures ranging from 100 K to 400 K. It is found that the experimental $C_v$ also increases with the increasing temperature, but this amplitude of variation is very tiny. Its corner temperature may be lower than all theoretical corner temperatures. In addition, we can find that the experimental values have an error bar about ± 0.05 MJ/m$^3$ K, and the difference between our theoretical convergence constant at high temperature and the experimental ones is not over this error, indicating that our theoretical results are well consistent with these experimental values. From the inset of Fig. 6, we can also find that the theoretical results by thermal expansion data [42] are not convergent at the temperature from 100 K to 400 K, and its amplitude of variation is larger than ours. Thus, we believe that the obtained convergence constant value of $C_v$ by thermal expansion data [42] should be larger than ours, and our results are better consistent with the experimental data.

The mode-averaged Gruneisen parameter $\bar{\gamma}$[43] expressed in Eq. (13) can characterize the anharmonicity of a crystal. In Eq. (13), $C_\lambda$ and $\gamma_\lambda$ is the specific heat capacity and Gruneisen parameter per mode, and the latter are defined through the change in phonon-mode frequency with crystal volume [44]

$$\gamma_\lambda = -\frac{V}{\omega_\lambda}\frac{\partial \omega_\lambda}{\partial V}. \tag{15}$$

This can be expressed in terms of the phonon dispersions and the third-order force constant

$$\gamma_\lambda = -\frac{1}{6\omega_\lambda^2}\sum_{\kappa}\sum_{l'\kappa'}\sum_{l''\kappa''}\sum_{\alpha\beta\gamma}\Phi_{\alpha\beta\gamma}(0\kappa, l'\kappa', l''\kappa'') \times \frac{e_{\alpha\kappa}^{\lambda *} e_{\beta\kappa'}^{\lambda'}}{\sqrt{M_\kappa M_{\kappa'}}} e^{i\mathbf{q}\cdot\mathbf{R}_{l'}} r_{l''\kappa''\gamma}. \tag{16}$$

where $V$, $\omega_\lambda$, $r_{l\kappa\gamma}$ and $e_{\alpha\kappa}^{\lambda}$ are the volume, phonon frequency of mode $\lambda$, the $\gamma$-th component of the vector locating the $\kappa$-th lattice atom in the $l$-th unit cell and the $\alpha$-th component of the phonon eigenvector for atom $\kappa$ in mode $\lambda$. At room temperature, the specific heat capacity approaches to a constant, and thus the mode-averaged Gruneisen parameter $\bar{\gamma}$ can be approximated to the average of the Gruneisen parameter per mode $\gamma_\lambda$. The obtained $\bar{\gamma}$ are list in Table 2.

In Table 2, the theoretical data of the mode-averaged Gruneisen parameter is obtained based on the Leibfried and Schlömann theory [45,46], where the needed value of the thermal conductivity is from the experimental data [6]. The difference between other theoretical value of Gruneisen parameter and ours is due to the different calculation methods. The Leibfried and Schlömann theory depend mainly on the experimental thermal conductivity and Debye temperature, and our results are from the first-principles calculation without any experimental data. However, it is found that this difference between its results and ours are very tiny, as also confirms the reliability of our anharmonic IFCs calculations.

The convergence of the lattice thermal conductivity $\kappa_l$ with respect to the BZ sampling density with scalebroad =1.0 are shown in Fig. 7. Each set of points is fitted to a curve of the form $\kappa_l = \kappa_l|_{N_1\to\infty}[1 + e^{-N_1/A}]$, so that both the asymptotic value and the convergence rate can be estimated. In Fig. 7 the red diamonds and blue spheres represent our result from RTA and the iterative solution of BTE, respectively. The horizontal black dash line represents the experimental value [6]. In this particular case, our extrapolation of the lattice thermal conductivity $\kappa_l$ to $N_1\to\infty$ yields a value of 1.14 W/mK, well consistent with the experimental data, 1.01 W/mK, by Andersson et al.[6], and the result confirms the deduction described in Section 3.2. The thermal conductivity obtained from RTA is shown in Table 2. It is found that the RTA result is close to the result by the iterative solution of BTE, and agrees better with the experiment value than the iterative solution of BTE. The difference between RTA and the iterative solution of BTE is mainly due to the normal (N) scattering process. RTA indicates that the normal (N) scattering process can provide resistive manner, but this is

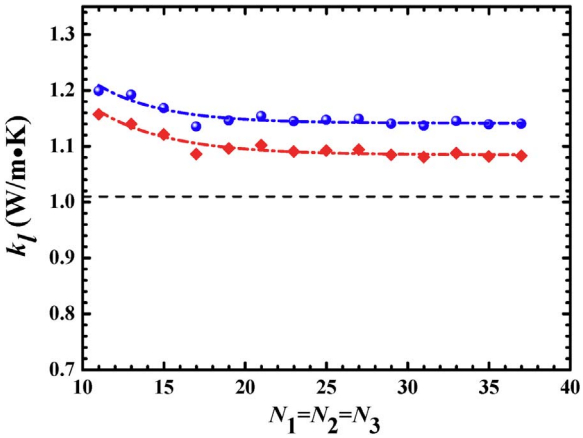


**Fig. 7.** Lattice thermal conductivity $\kappa_l$ of CsCl for different numbers of **q** points along each axis. Red diamonds and blue spheres are our results from RTA and our results with scalebroad =1.0 from the iterative solution of BTE, respectively. Solid lines are fits of each set of points to the function $\kappa_l = \kappa_l|_{N_1\to\infty}[1 + e^{-N_1/A}]$; Horizontal black line are the experimental value from Gerlich and Andersson [6]. (For interpretation of the references to color in this figure legend,the reader is referred to the web version of this article)

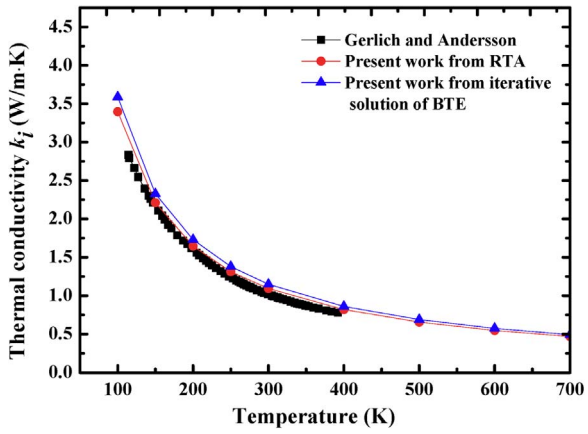


**Fig. 8.** Lattice thermal conductivity $\kappa_l$ of CsCl at different temperatures ranging from 100 K to 700 K. Red circles: our results from RTA; Blue triangles: our results from iterative solution of BTE with scalebroad =1.0; Black squares: experiment data by Gerlich and Andersson [6]. (For interpretation of the references to color in this figure legend,the reader is referred to the web version of this article)

contradicting with physical truth. In fact, the iterative solution of BTE is closely to real value by iterative calculation. The highly agreement between RTA and the iterative solution of BTE indicates that the umkalpp scattering process is main for CsCl crystal, and the normal (N) scattering process can be neglected. Furthermore the obtained thermal conductivity of CsCl is rather low, implying that CsCl has a strong umkalpp scattering process. This is similar to the analysis from Ward et al.[12] and Li and Mingo [47].

The lattice thermal conductivity of CsCl in temperature ranging from 100 K to 700 K are shown in Fig. 8 with a 27×27×27 k-grid in scalebroad=1.0 (There is a phase transition point for CsCl at around 740 K). We can see that the lattice thermal conductivity exponentially decreases with the increasing temperature $T$ at low temperatures, whereas it tends to be proportional to $1/T$ at high temperatures. Unfortunately, the experimental temperature range is only from 100 K to 400 K, so we can only make a comparison in this temperature range. Our results are slightly higher than the experimental results. The reliability of the second- and third-order IFCs has been demonstrated from previous analysis, so we infer that the tiny difference of the thermal conductivity between our results and the experimental data is due to a variety of minor scattering sources in the experiment samples, such as impurities, defects, residual isotopic disorder, and so on, especially the boundary effects at low temperatures. These minor scattering sources in experiment samples also play an important role to further induce the value of the thermal conductivity of CsCl, thus we believe that our results obtained by an iterative solution of the Boltzmann transport equation are rather reasonable.

## 4. Conclusions

The lattice thermal conductivity of CsCl crystal is successful calculated by first-principles theoretical approach based on an iterative solution of Boltzmann transport equation. The phonon spectrum, dielectric constants and the Born effective charges of CsCl are obtained from the density functional perturbative theory (DFPT). Our results show a great agreement with the experimental data and other theoretical results. The obtained heat capacity 1.28 MJ/m$^3$ K is also in good agreement with the available experimental data. Phonon mean free path, 9.4 nm, at 300 K is also presented, which is important for the study of size effect and nano-engineering. The RTA and iterative solution of BTE are both presented. The results show that both methods can obtain the thermal conductivity successfully.

## Acknowledgments

The authors would like to thank the support by the NSAF Joint Fund Jointly set up by the National Natural Science Foundation of China and the Chinese Academy of Engineering Physics (Grant Nos. U1430117, U1230201). Some calculations are performed on the ScGrid of Supercomputing Center, Computer Network Information Center of Chinese Academy of Sciences. We also acknowledge the support for the computational resources by the State Key Laboratory of Polymer Materials Engineering of China in Sichuan University.

## References

[1] S. Bingol, B. Erdinc, H. Akkus, Int. J. Simul. Multisci. Des. Optim. A 7 (2015) 6.
[2] G. Yoshikawa, M. Chi, K. Ueno, A. Koma, K. Saiki, Surf. Sci. 554 (2003) 220.
[3] S. Delpecha, C. Cabetb, C. Slima, G.S. Picarda, Mater. Today 13 (2010) 34.
[4] M.M. Waldrop, Nature 492 (2012) 26.
[5] Y. Ishii, K. Sato, M. Salanne, P.A. Madden, N. Ohtori, J. Phys. Chem. B 118 (2014) 3385.
[6] D. Gerlich, P. Andersson, J. Phys, C. Solid, State Phys. 15 (1982) 5211.
[7] R.E. Peierls, Ann. Phys. Lpz. 3 (1929) 1055.
[8] J.M. Ziman, Electrons and Phonons, Oxford University Press, London, 1960.
[9] S. Pettersson, J. Phys. C 20 (1987) 1047.
[10] J. Callaway, Phys. Rev. 113 (1959) 1046.
[11] P.B. Allen, Phys. Rev. B 88 (2013) 144302.
[12] A. Ward, D.A. Broido, D.A. Stewart, G. Deinzer, Phys. Rev. B 80 (2009) 125203.
[13] W. Li, J. Carrete, N.A. Katcho, N. Mingo, Comput. Phys. Commun. 185 (2014) 1747.
[14] M.D. Santia, N. Tandon, J.D. Albrecht, Appl. Phys. Lett. 107 (2015) 041907.
[15] L. Lindsay, W. Li, J. Carrete, N. Mingo, D.A. Broido, T.L. Reinecke, Phys. Rev. B 89 (2014) 155426.
[16] J.L. Ma, W. Li, X.B. Luo, Phys. Rev. B 90 (2014) 035203.
[17] Y.Y. Qi, T. Zhang, Y. Cheng, X.R. Chen, D.Q. Wei, L.C. Cai, J. Appl. Phys. 119 (2016) 095103.
[18] M. Omini, A. Sparavigna, Physica B 212 (1995) 101.
[19] M. Omini, A. Sparavigna, Phys. Rev. B 53 (1996) 9064.
[20] P.E. Blochl, Phys. Rev. B 50 (1994) 17953.
[21] S.H. Vosko, L. Wilk, M. Nusair, Can. J. Phys. 58 (1980) 1200.
[22] J.P. Perdew, Y. Wang, Phys. Rev. B 45 (1992) 13244.
[23] G. Kresse, J. Furthmüller, Phys. Rev. B 54 (1996) 11169.
[24] H.J. Monkhorst, J.D. Pack, Phys. Rev. B 13 (1976) 5188.
[25] S.N. Vaidya, G.C. Kennedy, J. Phys. Chem. Solids 32 (1971) 951.
[26] W.N. Mei, L.L. Boyer, M.J. Mehl, M.M. Ossowski, H.T. Stokes, Phys. Rev. B 61 (2000) 11425.
[27] S. Satpathy, Phys. Rev. B 33 (1986) 8706.
[28] K. Esfarjani, G. Chen, H.T. Stokes, Phys. Rev. B 84 (2011) 085204.
[29] T. Atsushi, T. Isao, Scr. Mater. 108 (2015) 1.
[30] A.A.Z. Ahmad, H.G. Smith, N. Wakabayashi, M.K. Wilkinson, Phys. Rev. B 6 (1972) 3956.
[31] D.A. Broido, L. Lindsay, T.L. Reinecke, Phys. Rev. B 88 (2013) 214303.
[32] L. Lindsay, D.A. Broido, T.L. Reinecke, Phys. Rev. Lett. 109 (2012) 095901.
[33] F. Favot, A.D. Corso, Phys. Rev. B 60 (1999) 11428.
[34] J.W. Hong, D. Vanderbilt, Phys. Rev. B 88 (2013) 174107.
[35] G.O. Jones, D.H. Martin, P.A. Mawer, C.H. Perry, Proc. Roy. Soc. A 261 (1961) 10.
[36] M. Born, K. Huang, Dynamical Theory of Crystal Lattices, Clarendon, Oxford, 1954.
[37] S. Baroni, R. Resta, Phys. Rev. B 33 (1986) 7017.
[38] W. Weber, Phys. Rev. B 15 (1977) 4789.
[39] Z. Guo, A. Verma, X. Wu, F. Sun, A. Hickman, T. Masui, A. Kuramata, M. Higashiwaki, D. Jena, T. Luo, Appl. Phys. Lett. 106 (2015) 111909.
[40] L. Lindsay, D.A. Broido, J. Phys.: Condens. Matt. 20 (2008) 165209.
[41] J. Carrete, N. Mingo, S. Curtarolo, Appl. Phys. Lett. 105 (2014) 101907.
[42] Y.S. Touloukian, R.K. Kirby, R.E. Taylor, P.D. Desai, Thermophysical Properties of Matter, Vol. 12, Thermal Expansion of Metallic Elements and Alloys, Plenum Press, New York, 1975.
[43] G.K.H. Madsen, A. Katre, C. Bera, Phys. Stat. Sol. A 213 (2016) 803.
[44] J. Fabian, P.B. Allen, Phys. Rev. Lett. 79 (1997) 1885.
[45] G. Leibfried, E. Schlömann, Nachr. Akad. Wiss. Göttingen, Math. Phys. Kl. 4 (1954) 71.
[46] G.A. Slack, Solid State Physics, Academic Press, New York, 1979.
[47] W. Li, N. Mingo, J. Appl. Phys. 114 (2013) 183505.